Implementation of generalized Harvey-Shack theory in light scattering from rough surfaces

M. Günöven,[1,2,3,*] H. Nasser,[2] M. Ünal,[1,4] Ö. Aytekin,[5] R. Turan,[1,2,4] and A. Bek[1,2,4]

[1]*Micro and Nanotechnology Program of Graduate School of Natural and Applied Sciences, Middle East Technical University, 06800, Ankara, Turkey*

[2]*Center for Solar Energy Research and Applications, Middle East Technical University, 06800 Ankara, Turkey*

[3]*KalyonPV Research and Development Center, Kalyon Güneş Teknolojileri Üretim A.Ş., 06909 Ankara, Turkey*

[4]*Department of Physics, Middle East Technical University, 06800 Ankara, Turkey*

[5]*Department of Electrical and Electronics Engineering, Kırklareli University, 39100 Kırklareli, Turkey*

(Received 31 December 2019; accepted 18 September 2020; published 15 December 2020)

We present a discrete implementation of generalized Harvey-Shack scalar scattering theory to calculate angular intensity distributions from height profiles of select randomly textured surfaces proposed for use in solar cells and covering a wide range of surface characteristics. We compare these calculations to high-resolution angular intensity distribution measurements. These comparisons suggest that the pupil function does benefit from an additional correction factor for rough surfaces containing lateral feature sizes on the order of the wavelength, which can be attributed to effective medium effects. Moreover, secondary interactions within the surface topography are shown to be a mechanism that partly redistributes scattered power, affecting angular intensity distribution results. These mechanisms emerge as the two main limitations of the Harvey-Shack scalar scattering theory in the far field, which nonetheless produces remarkable quantitative predictions.

DOI: 10.1103/PhysRevA.102.063521

I. INTRODUCTION

Light scattering at surfaces is an important phenomenon in numerous optical applications ranging from noncontact metrology [1], geophysical remote sensing [2], x-ray imaging and extreme ultraviolet (EUV) photolithography systems [3–5], and realistic rendering in computer graphics [6], to stray light rejection systems [7]. Particularly in thin-film solar cell applications, light scattering from textured interfaces with micron- to submicron-size lateral features is often a desirable characteristic to increase optical path length and light trapping inside active layers, leading to photocurrent enhancement. However, increasing surface roughness is often detrimental to the material quality of subsequent layers, and degrades the electronic performance of the device [8]. In order to optimize such textures, it is desirable to have a modeling approach which is accurate, computationally accessible, and relatively parameter free, to predict the angular distribution of light after scattering from randomly and/or orderly textured interfaces, with arbitrary roughness, into slabs of material of arbitrary thickness, arbitrary refractive index, and for arbitrary incidence angles.

Historically, the two main approaches to the problem of surface scattering based on some approximation of Maxwell's equations consisted of the Rayleigh-Rice small-amplitude vector perturbation theory [9–13], which remains valid for large scatter angles and incorporate polarization effects, but is limited to smooth surfaces ($\sigma/\lambda \ll 1$), and the Beckmann-Kirchhoff scalar scattering theory [14], which remains valid for rough surfaces but contains a paraxial approximation that limits its use to small incidence and scatter angles. Developments in small-amplitude perturbation theory using the reduced Rayleigh equation (RRE) method [15–20] have enabled the study of higher-order coherent localization and multiple scattering effects, albeit for sufficiently small slopes and at the cost of computational complexity. Derivatives of the former approach, including the work of Carniglia [21], together with earlier work by Bennett and Porteus [22], have been used for total integrated scatter or haze calculations [23], (i.e., the ratio of diffuse reflected or transmitted scatter to total reflectance or transmittance), where the paraxial limitation is not important. However, for many applications including solar cells, haze calculation alone is not always enough to give an accurate characterization of the scattering ability of a surface [24,25].

Rigorous methods that solve for Maxwell's equations have been used to model light scattering at randomly textured interfaces. These include methods such as rigorous wave coupled analysis (RCWA) [26,27] which divides the volume into homogeneous layers, the finite-difference time-domain (FDTD) [28,29] or finite-element method (FEM) [30] which discretize the entire volume, and surface integral methods such as the method of moments (MoM) [31] or the nonperturbative reduced Rayleigh equation (RRE) method [32–35]. While these rigorous numerical methods are important for validating applicability ranges of more approximate theories, they do not lend themselves well to parametrization for random textures, and they can become computationally intensive for statistically relevant large surfaces.

In this context, a particularly interesting method stems from the work of Harvey *et al.*, who over the years developed

*mete.gunoven@metu.edu.tr

a nonparaxial scalar scattering theory based on a Fourier optics linear-systems approach [36–40], suitable for both rough surfaces and large scatter angles. In Harvey-Shack scalar scattering theory (HS-SST), the optical phase accumulation across the texture zone is linked to statistical surface parameters such as roughness and autocorrelation function for well-behaved surfaces [3–6,36,41] or applied directly to a given surface topography [42–47], to model surface scatter in a wide range of applications, including solar cell research [41–47], for over a decade. These calculations have been incorporated in multilayer device simulations to model absorption and current enhancement in solar cells and other optoelectronic devices [44,45].

In this work, we present an implementation of generalized HS-SST for angular intensity distribution (AID) calculation from isotropic textures, that takes advantage of the azimuthal symmetry in the Fourier transform of their height profiles. We compare computational results from select solar cell surface textures covering a wide range of surface characteristics to actual high-resolution far-field intensity measurements to validate our approach. In light of these comparisons, we propose an additional correction factor to the Fourier-transformed phase accumulation to incorporate effective medium effects to the HS-SST model, which start to become relevant for rough surfaces as the lateral feature sizes become comparable to the wavelength. Furthermore, we show that secondary interactions within the surface topography constitute a mechanism that partly redistributes scattered power, affecting AID results compared to HS-SST predictions.

II. EXPERIMENTAL PROCEDURE

A. Sample preparation and surface parameters

Two different types of samples, covering a wide range of surface roughness (σ) and lateral autocorrelation lengths (acl) were used in this study. Tapping-mode atomic force microscope (AFM) topography images from $25 \times 25\,\mu\text{m}^2$ areas with 256 data points per line, and corresponding height and slope angle distribution statistics, are provided in Fig. 1. The acl and σ values, extracted using GWYDDION software [48] after plane subtraction for tilt correction, are provided in Table I. Slope distributions were obtained using local plane fitting around each data point.

Samples A and B were prepared using the aluminum induced texturing (AIT) method [49], where a 150-nm-thick layer of aluminum is deposited, using thermal evaporation, on 3-mm-thick soda-lime glass substrates (refractive index $n = 1.52$), annealed at 600 °C for 60 min to produce a textured Al_2O_3 layer with Si precipitates at the interface, which is then etched using successive H_3PO_4 and $HF : HNO_3$ solutions (sample A) [50] or a $NaOH : H_2O_2 : H_2O$ solution (sample B) [51], for different etch durations. The presence of intermediate Si precipitates creates a larger length scale superimposed on an optically relevant smaller length scale. This small texture manifests itself as a micron-sized, craterlike texture for sample A, and a finer, pyramidlike texture for sample B, ranging from smooth to moderately rough surfaces. The radial autocorrelation function (ACF) is best modeled using a two-Gaussian fit $[f(x) = \sigma_1^2 e^{-(x/acl_1)^2} + \sigma_2^2 e^{-(x/acl_2)^2}]$. For these samples, the optically relevant smaller autocorrelation length and corresponding roughness values are indicated with an asterisk. Samples C and D were prepared by depositing 1.25-μm-thick Al:ZnO by sputtering on 2-mm-thick flat Schott glass substrates, followed by wet HCl etching [52] for 30 s, at different concentrations. Ellipsometry analysis indicates a refractive index of $n = 1.87$. The rougher textures produced by this method present a highly uniform distribution of "etch pits," resulting in a height distribution with a negative skew. The radial ACF is ideally modeled using a single Gaussian fit $[f(x) = \sigma^2 e^{-(x/acl)^2}]$, leading to small autocorrelation lengths.

B. Angular intensity distribution measurements

AID of light scattering from these samples was measured using a purpose-designed homemade automated goniometer system. This instrument, as illustrated in Fig. 2(a), consists of two concentric rotation stages. The first one in the center supports a screen with a 3-mm-diameter aperture that holds the sample and controls the angle of incidence. A laser beam of fixed path, with 532-nm wavelength and a 1.5-mm Gaussian beam waist traverses the center of this aperture, after being modulated by an optical chopper. In this work, only *s*-polarized incident light is used.

The second stage controls a detector arm that rotates around the center independently of the first stage, and scans for scatter signal in either reflection or transmission. On the detector arm, scattered light is coupled to a 1-mm core diameter optical fiber through a 3-mm-diameter diffuser film at a distance of 244 mm from the center aperture; this corresponds to a light-collecting area of $\Delta\Omega s = 1.2 \times 10^{-4}$ sr. This small collector footprint ensures very little blocking of incident light around the incidence direction in reflection measurements (<2° wide), while being adequate to collect the entire laser beam power when it is directly incident on the collector, thus minimizing beam convolution effects. The other side of the fiber is coupled to a silicon photodetector, whose signal is measured using a lock-in amplifier. The center aperture diameter, in conjunction with laser beam width and sample thicknesses, is selected to be able to reject the effect of multiple reflections inside the glass substrate for 30° and 60° incidence measurements, as illustrated in Fig. 2(b). The scatter signal is then normalized by the incident beam signal (laser beam measured directly by the same collector without sample) and by the subtended solid angle, to obtain the normalized AID in the plane of incidence, expressed in sr^{-1}. Samples are considered to be nonabsorptive at this wavelength. In transmission measurements, the reflection loss at the first flat surface is accounted for by dividing the signal by the corresponding Fresnel coefficient.

III. ANGULAR INTENSITY DISTRIBUTION CALCULATION

A. Review of Harvey-Shack scalar scattering theory

HS-SST uses the Fourier transform of the optical phase that light accumulates while traversing the rough surface texture, to evaluate the far-field approximation of the Rayleigh-Sommerfeld diffraction integral observed on a hemisphere

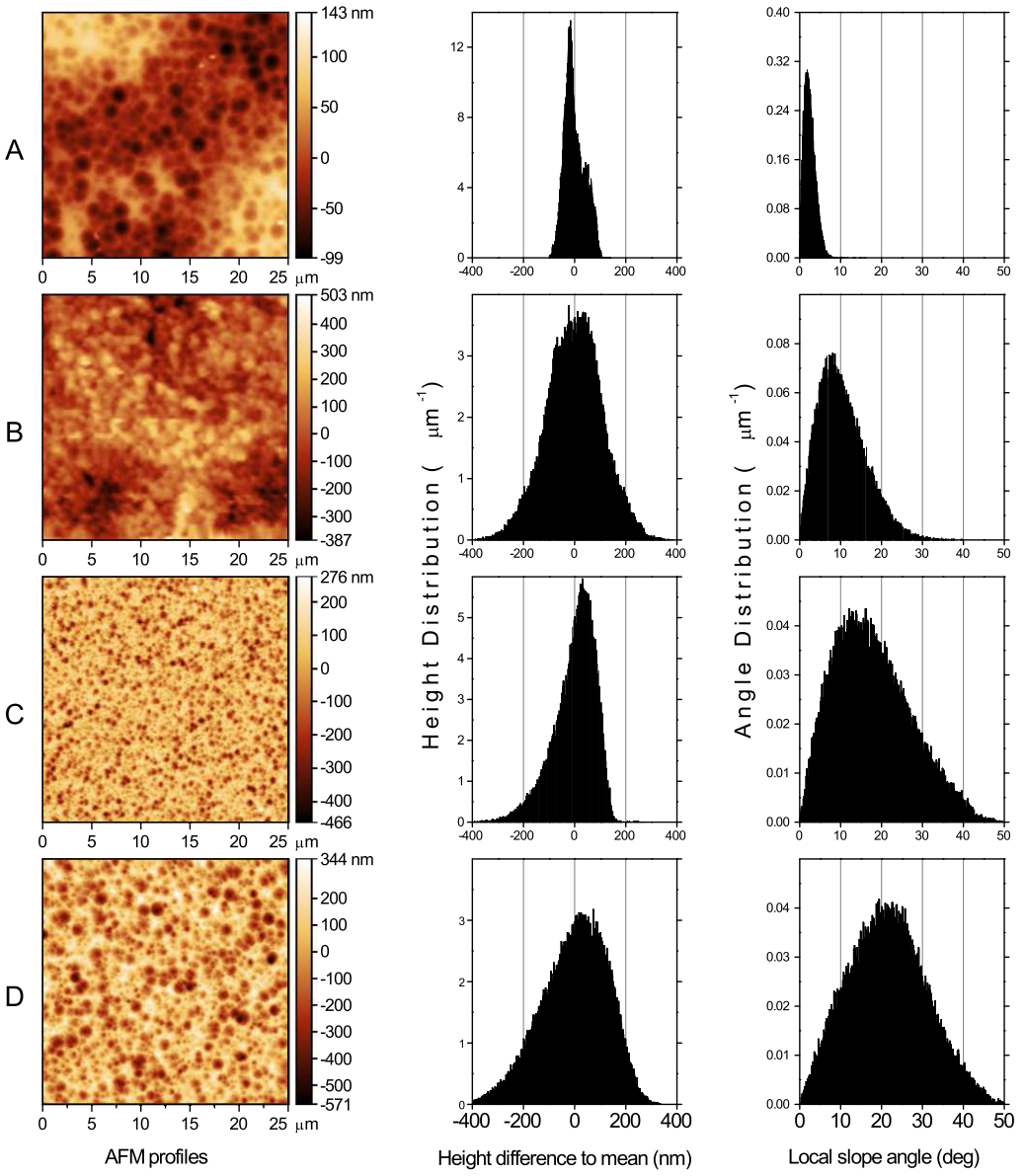

FIG. 1. AFM images, height, and slope angle distributions.

centered around the sample aperture. This resulting radiant power distribution in direction-cosines space can be expressed as

$$\phi(\alpha, \beta - \beta_0) = K_{\text{norm}} \, |\mathcal{F}\{U_0(\hat{x}, \hat{y}; 0)\, e^{i2\pi\beta_0\hat{y}}\}|^2. \qquad (1)$$

In this expression, $\hat{x}$, $\hat{y}$ are the wavelength-normalized coordinates of the aperture plane, α and β are the direction cosines, and β_0 contains the shifting effect due to an oblique incidence along one of the directions. U_0 is the complex amplitude distribution caused at the aperture, which consists of only phase changes for a nonabsorbing textured surface [53]. K_{norm} is a normalization factor that redistributes the power contained in evanescent waves ($\alpha^2 + \beta^2 > 1$) back into radiant modes:

$$K_{\text{norm}} = \begin{cases} \dfrac{\int\int_{-\infty}^{+\infty} |\mathcal{F}\{U_0(\hat{x},\hat{y};0)\, e^{i2\pi\beta_0\hat{y}}\}|^2 d\alpha d\beta}{\int_{\alpha=-1}^{1} \int_{\beta=-(1-\alpha^2)^{1/2}}^{(1-\alpha^2)^{1/2}} |\mathcal{F}\{U_0(\hat{x},\hat{y};0)\, e^{i2\pi\beta_0\hat{y}}\}|^2 d\alpha d\beta}; & \alpha^2 + \beta^2 \leqslant 1 \\ 0 & \alpha^2 + \beta^2 > 1 \end{cases} \qquad (2)$$

For a homogeneously illuminated, nonabsorbing rough textured surface with homogeneous reflectance and transmittance U_0, the complex amplitude distribution caused by the

TABLE I. Surface roughness σ and autocorrelation length acl extracted from AFM topography images.

	A	B	C	D
σ (nm)	20.4*	69.6*	82.7	129.4
acl (nm)	859*	618*	321	527

*indicate optically relevant smaller acl and σ values.

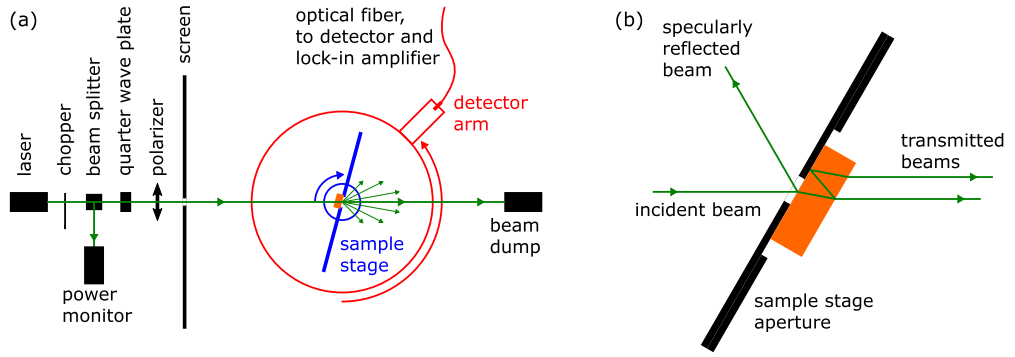

FIG. 2. (a) General schematic of instrumentation, shown for AID in transmission measurement. (b) Aperture width and sample thickness minimizing multiple reflection effects, shown for AID in reflection measurement.

aperture, can be expressed as

$$U_0(\hat{x}, \hat{y}; \gamma_i, \gamma_s, \hat{z} = 0) = \sqrt{p_i\, f_{R,T}}\; e^{i2\pi(\gamma_i n_i \pm \gamma_s n_s)\,\hat{h}(\hat{x},\hat{y})}, \quad (3)$$

where p_i is the incident power, $f_{R,T}$ is the fraction of power reflected or transmitted through the surface and is given by the respective Fresnel coefficients for a flat surface, γ_i and γ_s are the cosines of the angles of incidence and scattering as illustrated in Fig. 3, n_i and n_s are the refractive indices of the medium of incidence and the medium into which scattering occurs, and $\hat{h}(\hat{x}, \hat{y})$ is the wavelength-normalized surface height profile. The plus sign is used for scattering in reflection, where $n_i = n_s$ also; the minus sign is used for scattering in transmission.

The use of the pupil function given in Eq. (3) was introduced by Krywonos *et al.* [39,40] and is the characteristic that defines the *generalized* HS-SST. When applied to a surface featuring a single facet angle, this pupil function correctly predicts the refraction angle [47]. The earlier, original version of the theory [3,6,36,41–46] that makes use of a simpler pupil function omitting the angular dependence of the path difference does not have this property [46,47]. It should be noted that because this pupil function depends on the scatter angle, the Fourier transform is accurate only for the amplitude corresponding to that particular scatter angle. For any given incidence angle, a single Fourier transform is hence not sufficient to calculate the complex amplitude and angular power distributions. The implementation is therefore more computationally intensive, as it requires multiple Fourier transforms to reconstruct the scattered intensity and power distributions.

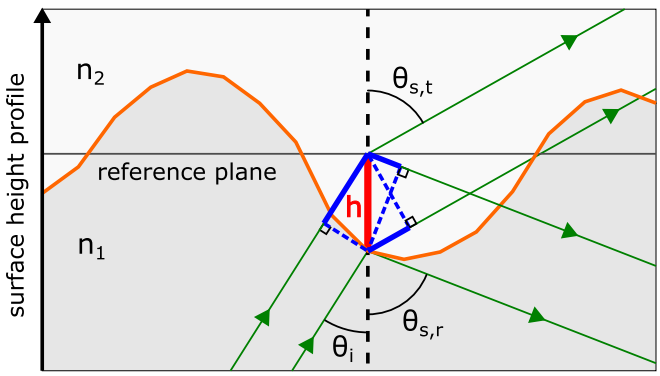

FIG. 3. Optical path difference induced on a light ray by the texture, compared to a flat plane.

B. Discrete implementation

Here we describe our implementation, which uses elements from a series of discrete two-dimensional (2D) fast Fourier transform (FFT) algorithms to reconstruct the AID, generalizing the stitching method [47] used by Haug *et al.* The FFT operations are performed, one for each different scatter angle, on the optical phase accumulated as light traverses the surface on grid points corresponding to the AFM data points. The discrete equivalent of Eq. (1) for normal incidence can be expressed as

$$\frac{P_{\alpha,\beta}}{p_i} = K_{\text{norm}}\, f_{R,T} \left| \frac{\text{FFT}_{2D}\{e^{i2\pi(\gamma_i n_i \pm \gamma_s n_s)\hat{h}(N\times N)}\}}{N^2} \right|^2. \quad (4)$$

An AFM scan of side length L generates a height profile $\hat{h}$ taken on $N \times N$ discrete points at regular intervals across the surface. Since the modulus of each exponential is unity, and there are N^2 of them, we make use of Parseval's theorem to normalize the sum of the FFT elements by dividing it by N^2. The result of this 2D FFT operation, represented in Fig. 4(a), is composed of $N \times N$ matrix elements that do not contain information on lateral coordinates. These lateral coordinates can be assigned by regarding the AFM image as a 2D crossed diffraction grating with groove period L in either direction. For simplicity, consider the grating equation along one axis:

$$\frac{n_i}{n_s} \sin\theta_i + m\frac{\lambda}{L\, n_s} = \sin\theta_s, \quad (5)$$

where the integer m is the diffraction order. At normal incidence, the power of the nondiffracted beam corresponding to the order $m = 0$ will be given by the central element ($\alpha = \beta = 0$), colored in Fig. 4. This central element corresponds to the zenith direction of the hemisphere. The width of this central element, as well as the distance between each consecutive order on any axis in direction-cosines space, is given by $\Delta\alpha = \Delta\beta = \lambda/(L\, n_s)$, and corresponds to the low spatial frequency limit of the AFM measurement. The power $P_{\alpha,\beta}$ contained in an element of discrete coordinates (α, β) can be thought of as distributed on a $\Delta\alpha \times \Delta\beta$ area centered around these coordinates. The high spatial frequency band limit of the AFM measurement [determined by the distance

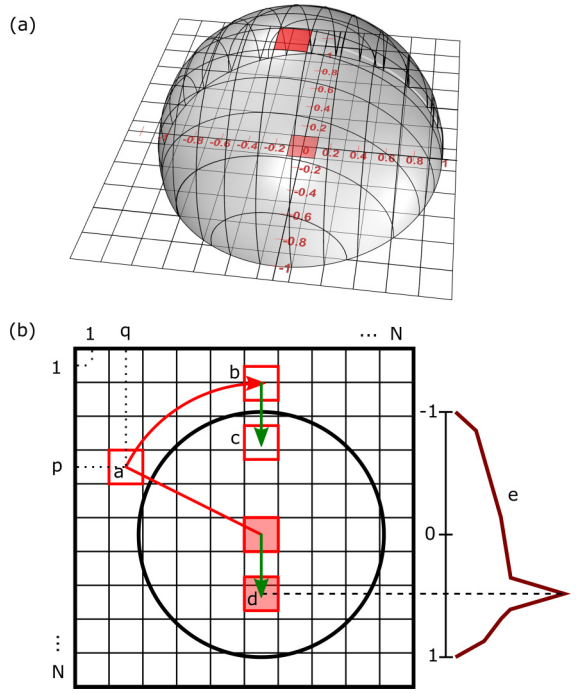

FIG. 4. (a) 2D FFT operation, its associated diffraction hemisphere, and direction-cosine coordinates. (b) Azimuthal projection algorithm for isotropic samples. (a) Position of an element with respect to the unshifted center in 2D space. (b) Because of circular symmetry, only the radial distance of elements needs to be considered, reducing the problem to one dimension. (c) Applying the shift due to the angle of incidence. (d) Position of the nondiffracted beam. (e) Resulting AID, after dividing the power in each element by the corresponding solid angle (with respect to the shifted center).

between each scan point (i.e., L/N)] is not very crucial, as these frequencies usually correspond to evanescent waves. However, care should be taken to select a large enough grid size N, so that the diffraction hemisphere does not brim over the image grid for oblique incidence angles and smaller wavelengths. Since only the matrix elements with a radial distance (in direction-cosine space) to this central element such as $\alpha^2+\beta^2 \leqslant 1$ are propagating, the radius of the propagation hemisphere consists of $1/\Delta\alpha$ matrix elements. The shifting effect due to oblique incidence can be incorporated in the 2D power distribution map by using the $e^{i2\pi\beta_0\hat{y}}$ term in the FFT, just as in the analytical expression, but doing this generally splits the power contained in the nondiffracted beam into two matrix elements [unless the shift, $n_i/n_s\sin(\theta_i)$ happens to be an exact multiple of $\Delta\alpha$]. We prefer instead to shift the coordinates of the observation hemisphere along one of the axes, and calculate radial distances from that shifted center.

For isotropic surfaces where we can take advantage of the circularly symmetric power distribution around the central element, we use the azimuthal projection algorithm illustrated in Fig. 4(b) to calculate the AID under oblique incidence. For each matrix element, the radial distance in direction-cosines space, $d_0=\sqrt{\alpha^2+\beta^2}$, to the unshifted central element is calculated. Each element is doubled to contribute one positive and one negative distance. The shift amount, $s=n_i/n_s\sin(\theta_i)$, is then added to all these distances. Thus, among $N\times N$ elements, only those $(p,\ q)$ whose shifted distances, $d=\pm d_0+s$, fall within $[-1,\ 1]$ on the axis of the oblique incidence in direction-cosine space correspond to valid scatter angles. The FFT operation in Eq. (4) is performed for each of these elements $(p,\ q)$ using their corresponding scatter angle cosines γ_s, and in the result, only the value of the element $(p,\ q)$ is retained, associated to shifted distance $d=\sin\theta_s$. The radiant angular power distribution is reconstructed element by element, after scanning for all valid elements mapping to within $[-1,\ 1]$.

Finally, to obtain the intensity distribution along the direction of the oblique incidence, the power diffracted into each reconstructed element is divided by its corresponding solid angle $\Delta\Omega_{\alpha,\beta}\cong\Delta\alpha\ \Delta\beta/\gamma'$, where $\gamma'=\cos(\sin^{-1}d)$, d being the shifted distance:

$$\frac{I_{\beta,\beta_0}}{p_i}=K_{\text{norm}}\ f_{R,T}\times\text{Proj.}_{2\text{D}\to1\text{D}}\left\{\left|\frac{\text{FFT}_{2\text{D}}\left\{e^{i2\pi(\gamma_i n_i\pm\gamma_s n_s)\hat{h}(N\times N)}\right\}}{N^2}\right|^2\right\}\Big/\Delta\Omega_{\alpha,\beta},\tag{6}$$

where $\text{Proj.}_{2\text{D}\to1\text{D}}$ with brackets denotes the element-by-element projection reconstruction algorithm.

Note that using the *generalized* HS-SST pupil function, complex amplitudes corresponding to evanescent modes lying outside the unit circle are undefined. However, due to the conservation of energy, the sum of the normalized power distribution inside the unit circle (before applying the $f_{R,T}$ term), should be equal to unity. After calculating the 2D radiant power distribution inside the shifted propagation hemisphere, K_{norm} can still be defined as the inverse of the total radiant power contained inside the unit circle:

$$K_{\text{norm}}=\frac{1}{\sum_{\alpha^2+\beta^2\leqslant1}\text{Reconstruct}_{2\text{D}}\left\{\left|\frac{FFT_{2\text{D}}\left\{e^{i2\pi(\gamma_i n_i\pm\gamma_s n_s)\hat{h}(N\times N)}\right\}}{N^2}\right|^2\right\}},\tag{7}$$

where the term in brackets denotes another element-by-element reconstruction operation, without projection. In order to render the AID graph more comprehensible, we use a smoothing algorithm that averages data points that fall into angle bins, the width of which is taken to match the angular opening of our goniometer detector area of $\sim0.7°$, to reflect a similar angular integration effect. The intensity of the nondiffracted beam is not affected by this smoothing. With this algorithm, the isotropy of the sample can be exploited to obtain well-averaged AID results. Overall, this approach is computationally demanding due to the sheer number of operations, but can still be handled by a personal computer with ease, thanks to the high speeds of FFT algorithms.

IV. RESULTS AND DISCUSSION

AID calculations with respect to scatter angle $\theta_s=\sin^{-1}\beta$ are given in Fig. 5, and compared to angular measurements. Overall, the *generalized* HS-SST model shows remarkable experimental quantitative agreement for all samples. AIT glass samples (A, B) have relatively low surface roughnesses and large autocorrelation lengths; consequently they have strong light scattering close to the nondiffracted beam direction but

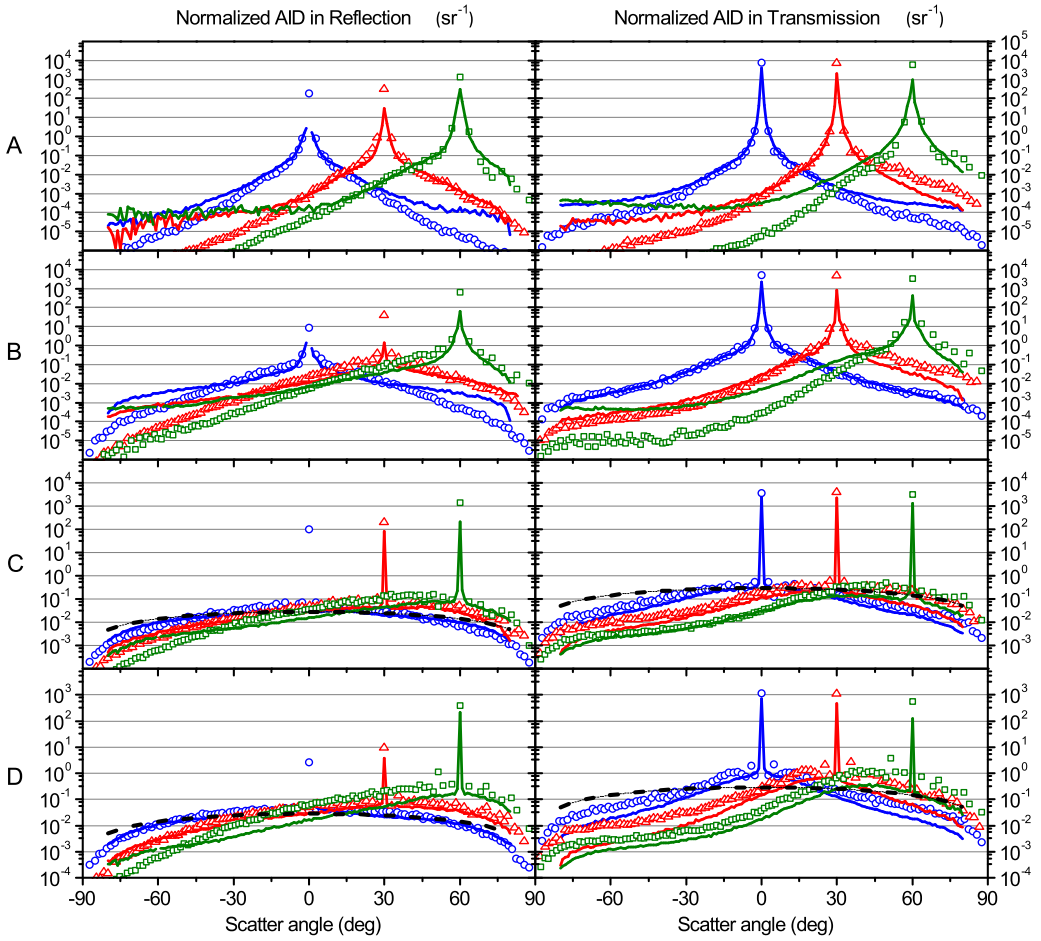

FIG. 5. AID in reflection (left) and in transmission (right), respectively, for specular and refraction angles of 0°, 30°, and 60°. Symbols represent calculations according to Eq. (6); solid lines represent measurements. For reflection calculations, incidence is through air; for transmission, incidence is through glass ($n = 1.52$, for samples A, B) or Al:ZnO ($n = 1.87$, for samples C, D). Lambertian AID (weighted by $f_{R,T}$), characterized by a constant power distribution in direction-cosine space, is given in dashed lines for reference.

weak scattering into higher angles, both in reflection and in transmission. Consequently, measured intensities for sample A clearly drop below the noise limit of the instrument, especially in reflection. Textured Al:ZnO samples (C, D) have higher surface roughness and smaller autocorrelation lengths, with steeper local angles and feature sizes comparable to or smaller than the measurement wavelength; consequently they have strong light scattering into higher angles, superimposed to a distinct nondiffracted beam that still contains a large portion of the reflected or transmitted power.

However, two notable deviations remain: Firstly, for AIT glass samples, calculated intensities for oblique incidence in both reflection and transmission fall steadily toward negative scatter angles (which we refer to as the backscattering direction), while measurements show a plateau, which is clearly over our instrument's noise level in most cases. This plateau is already evident in normal incidence transmission for sample A, above scatter angles around 45°. Similar plateaus manifest themselves in AID measurements of related works in the literature [45]. Moreover, for AIT glass samples, calculated intensities in the forward scattering direction around and beyond the nondiffracted beam angle appear to be overestimated, especially in transmission. Secondly, for Al:ZnO samples, the magnitude of the calculated intensity distribution also exhibits a relative decrease in the backscattering direction when compared to measurements, but this is compounded by another distinct, second deviation: The diffuse parts of the calculated intensity distributions are noticeably shifted up compared to their measured levels. We discuss possible explanations about these observations in the following sections.

A. Effective medium correction factor

The persistent overestimation of diffuse intensity compared to measurements for Al:ZnO samples with relatively rough surfaces and small lateral autocorrelation lengths suggests that the phase screen that is Fourier transformed in Eq. (6) could be too dense. Other factors specific to Al:ZnO samples, such as scattering caused by residual roughness in the nominally flat glass-Al:ZnO interface, would all have the opposite effect of greater scattering into high angles in measurements.

Here, we propose a correction factor c to modify the pupil function of Eq. (3), such that $c < 1$, which results in a better

TABLE II. Empirical correction factors for normal incidence transmission, obtained using a dichotomous search optimization. Correction factors calculated using AID curves one standard deviation lower and higher are indicated in brackets. Relevant surface characteristics are also indicated.

	A	B	C	D
σ_{tot} (nm)	20.5*	70.0*	82.7	129.4
acl (nm)	889*	768*	321	527
Most likely local angle (deg)	2.0°	7.5°	14°	23°
Optimized c factor	1.175 [0.975;1.325]	0.950 [0.825;1.075]	0.750 [0.600;0.900]	0.575 [0.425;0.750]

*indicate optically relevant smaller acl and σ values, as explained in the experimental procedure.

empirical match with the measurements:

$$U_{0;\text{GHS}}(\hat{x},\hat{y};\gamma_i,\gamma_s,0) = \sqrt{p_i\, f_{R,T}}\; e^{i2\pi(\gamma_i n_i \pm \gamma_s n_s)\, c\, \hat{h}(\hat{x},\hat{y};0)}. \quad (8)$$

In order to estimate the correction factors that result in an optimal fit between calculations and measurements, we ran a dichotomous search algorithm. For normal incidence transmission, numerous scatter measurements were repeated from different locations across each sample, resulting in statistical variations at each scatter angle. These variations result from uncertainties due to instrumentation as well as the stochastic nature of the surface scattering phenomenon itself. Intensity values calculated using the empirical pupil function given in Eq. (8) were interpolated at measurement angles, and the squared difference between these two intensities was multiplied by $|\sin\theta_s|$. This is because for a sample with isotropic surface texture at normal incidence, the quantity $I(\theta_s)|\sin\theta_s|$ is proportional to the total intensity scattered across the entire hemisphere at a radial angle θ_s, not just a cross section of it as in angular measurements [24]. The peak values, where experimental uncertainties are greatest, are not taken into account. The c value resulting in the least total residual error was determined after several iterations. This dichotomous parameter search was repeated using curves one standard deviation lower and higher than the average AID, to give an estimation of the variability range of the correction factor. These optimized c factors and their expected range are given in Table II, together with other relevant surface parameters.

Correction factors for AIT textured glass samples with broad textures are close to unity, as expected. Deviations, such as $c = 1.175$ seen for sample A, probably result from AFM images not being representative enough of these samples, which might have limited homogeneity at this length scale owing to their larger features. Note that even for sample A, the expected $c = 1$ falls within the experimental error range. Furthermore, since these samples have high-intensity distributions close to the nondiffracted beam, slight experimental deviations in those few data points can offset the optimization result. Correction factors for both Al:ZnO samples are significantly less than 1, with sample D exhibiting the steepest angles that require the smallest factor. AID calculations with optimized c factors are shown in Fig. 6. Also included are transmission calculations with correction factors for refraction angles of 30° and 60° (calculated without the $|\sin\theta_s|$ multiplier to intensity), but the dichotomous search fitting is less reliable in oblique incidence, due to the compounding effect of the secondary interactions on the measured AID, which are visited in the next section.

A possible physical explanation for this behavior could be the onset of effective medium effects, which are not taken into account in scalar scattering theory. These samples exhibit moderately large vertical and small lateral features compared to the wavelength in the material, resulting in relatively steep local surface angles. The incident light around the peaks and pits of these textures experiences a gradual refractive index change, resulting in less overall optical phase accumulation compared to a texture with abrupt refractive index change. This would manifest as a reduction in the effective height profile of the roughness zone, and hence a correction factor smaller than unity.

Consider hypothetical pyramidal textures as illustrated in Fig. 7: (a) features a steep facet angle with a large base, corresponding to the geometric optics regime. (b) contains small heights with dimensions at the order of the wavelength and large lateral features (similar to sample A). It has slow phase accumulation due to shallow slopes, which results in weak scattering at high angles. (c) features a facet angle identical to (a); however, it has small heights at the order of the wavelength as in (b), but with smaller lateral features. Even though the phase accumulation *on each facet* is identical to that of (a), there are numerous regions with comparatively small phase change *around the tips and pits*, which translate to reduced high-frequency content in the Fourier transform when compared to (a). Moreover, (c) is more susceptible to effective medium approximation due to reduced feature dimensions, such that the effective height profile, suggested by the dotted lines in Fig. 7, starts to decrease compared to the actual profile around the tips and pits (i.e., a correction factor smaller than unity), which also decreases high-angle scattering. According to Eq. (6), in order to enhance high-angle scattering from a small texture, facet angles could be increased as in (d), similar to samples C and D with their skewed height distribution. However, a pronounced reduction of effective height profile due to effective medium effects opposes this enhancement, which explains the decreasing correction factor for samples B–D.

This limitation of *generalized* HS-SST arguably points toward a physical limitation of maximum achievable high-angle scattering inside absorber materials using surface texturing. If the roughness zone between the material and air acts like a graded medium, another consequence would be a decrease in reflectivity (and increase in transmissivity) compared to that given by Fresnel coefficients for a flat interface. This change

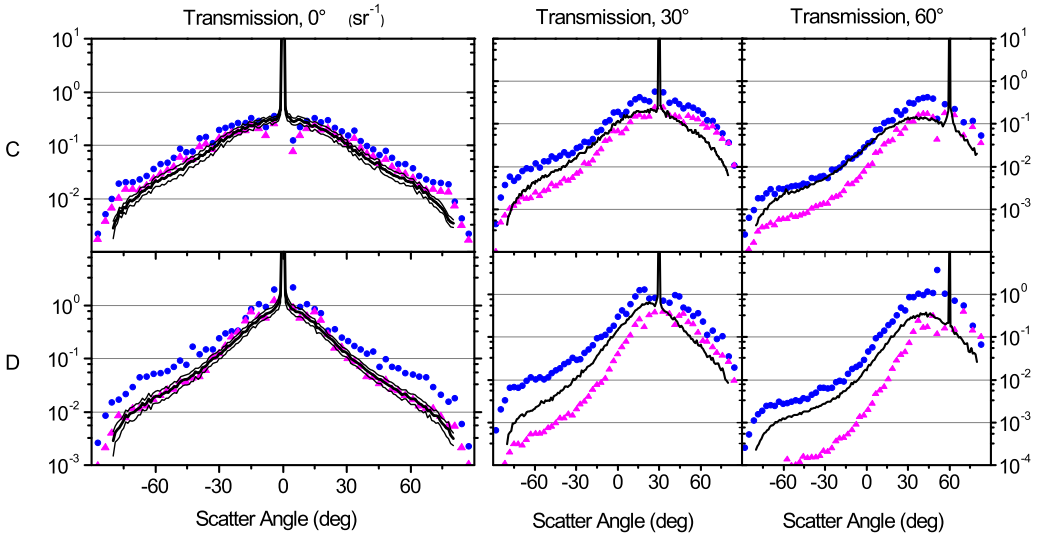

FIG. 6. AID in transmission, for samples C and D, for refraction angles of 0°, 30°, and 60°. Blue dots correspond to calculations without correction factors, while pink triangles correspond to calculations using correction factors given in Table II, optimized for fitting to measurements (black lines). Measurements in normal incidence transmission are shown with surrounding standard deviation intervals.

is proportionally more pronounced in reflection, which, together with backside reflected intensity in normal incidence measurements, complicates a similar dichotomous search of correction factors for reflection. Effective medium approximation is a complicated phenomenon, and an associated correction factor, if confirmed, would likely be a complicated function of the autocorrelation length, surface roughness, and refractive indices as well as the local surface geometry (volume fraction and distribution of local angles). We acknowledge that the uncertainties inherent in the metrology of AID measurements are not insignificant, and further investigations with a greater range of samples and shorter wavelength lasers are needed to confirm the existence of an effective medium correction factor.

B. Effects of secondary interactions

Another general limitation of scalar scattering theory is that it concerns only primary interactions of incident light with the surface. As such, shadowing events and secondary interactions at the surface topography are not considered. A possible explanation for the increased backscattering and reduced forward scattering observed across the samples is a redistribution of part of the scattered power due to the presence of such secondary interactions. This broad backscattering enhancement is distinct from the localized, coherent retroreflection phenomenon predicted by higher-order small-amplitude perturbation approaches [31–33]. The angle between a local facet plane and light scatter direction decreases with a high content of surface slope angles and with increasing scatter angle, rendering a secondary interaction more likely, in which scattered light reflects off another adjacent surface topographic feature. A similar argument can be made with increasing incidence angles and the probability of shadowing events, where a tall local surface feature blocks light from reaching the average surface plane. While it is not possible to know the effects of such interactions without performing rigorous calculations on well-defined surface geometries, it can be suggested that a secondary interaction tends to spread out the power contained in affected (forward) directions to all scatter directions more or less equally. Since for a random texture, the forward scatter direction close to the nondiffracted beam contains much more scattered power, a slight redistribution away from this direction could compensate for a large relative increase across all backscatter directions.

Notably, these scatter events do not take place only on the plane of incidence (which is the plane of our measurements), they affect the light scattered in any azimuthal direction with similar probability. A small part of this light undergoing secondary interaction across a different azimuthal direction could scatter back in the plane of incidence and be detected by the scanning detector. However, unlike primary scatter-

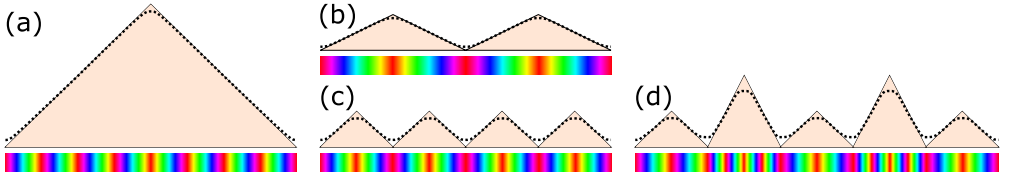

FIG. 7. Phase accumulation on pyramid facets with different facet angles and sizes. Colors stand for the optical phase accumulated when light traverses each profile. Dotted lines suggest an equivalent height profile, encompassing effective medium effects.

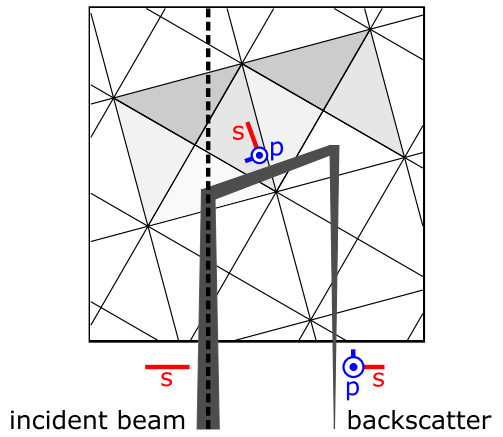

FIG. 8. Illustration of secondary interactions on a pyramidlike surface texture, top view.

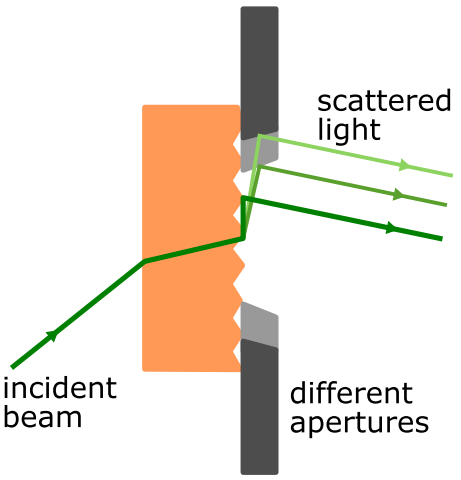

FIG. 10. Side view of sample aperture illustrating a secondary interaction from the surface topography (dark green line) or sides of the aperture with different radii (lighter green lines).

ing in the plane of incidence, such interactions involving other azimuthal directions would result in a change in the polarization direction of the detected light, as illustrated in Fig. 8.

To test this hypothesis, we have repeated some of our scatter measurements with a polarizer placed in front of the scanning detector. These AID results are given in Fig. 9, and exhibit a proportional increase of intensity measured with the *p* polarizer in the backscattering direction (or toward high angles for normal incidence) and reduction of intensity measured with the *s* polarizer. This observation is in line with the possible presence of secondary interactions that could explain the backscattering plateaus in our measurements in Figs. 5 and 6.

However, it is also possible that the observed polarization changes have a nontopographic, experiment-related source. For example, such secondary scattering events could also happen on the sides of the small aperture surrounding the sample surface, as illustrated in Fig. 10. In order to check for this instrumentation effect, the previous measurements were repeated using apertures of different diameters, 3 and 6 mm. The sides of a larger-diameter aperture, that has the same thickness as a small-diameter one, subtends a smaller solid angle with respect to the incident beam area, and therefore should produce fewer secondary interactions, if nontopographic secondary scattering is predominant.

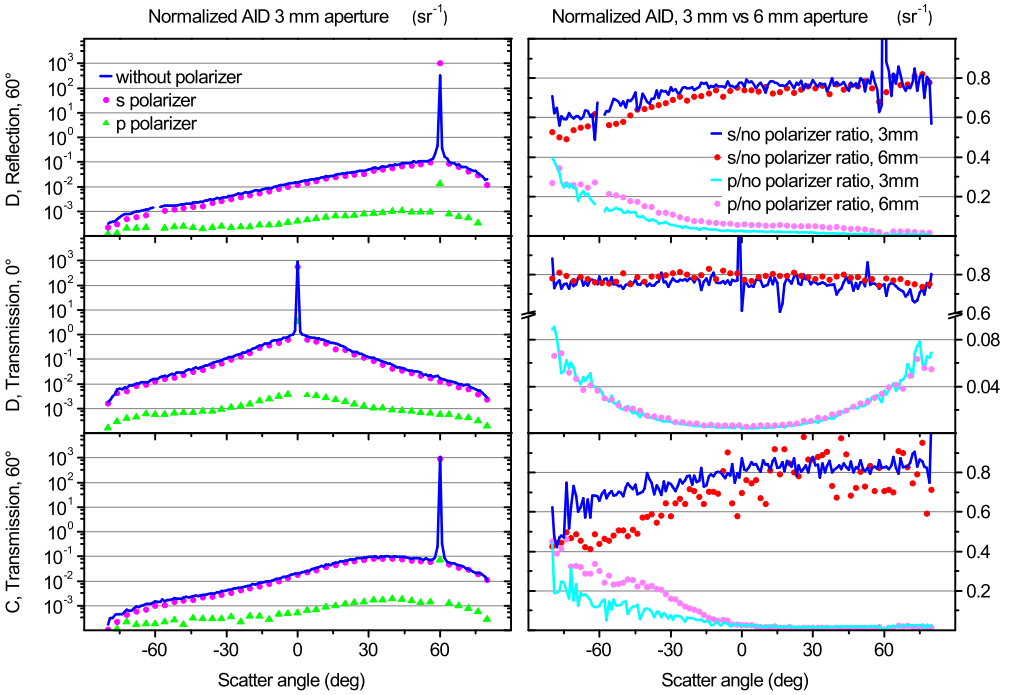

FIG. 9. Left: AID measurements with *s* polarizer (dots), *p* polarizer (triangles), and without polarizer (solid lines) in front of the detector (incident beam is *s* polarized). Right: *s*/no polarizer and *p*/no polarizer ratios, measured using 3- and 6-mm-diameter aperture sizes.

The resulting *s*/no polarizer and *p*/no polarizer intensity ratios are given in Fig. 9 (right), which display little difference. This confirms that secondary interactions are indeed originating from the surface topography. From a purely geometric optics perspective, the effect of secondary interactions should be negligible for the small slopes composing our samples. The redistribution of power to all combined backscatter directions should indeed make up a small percentage of the overall radiated power, which is concentrated mainly near the nondiffracted beam direction, but the effects are still detectable, and the superposition makes precise quantitative interpretation of low-level scattering difficult. While it is not possible to integrate these effects directly into the pupil function, it might be possible to add them to the 2D power distribution map heuristically. In samples where these effects are dominant, such as those with large anisotropic features, scalar scattering theory should be supplemented by ray tracing or other rigorous methods.

V. CONCLUSION

Accurate modeling of light scattering from textured optical thin films is an important aspect of light management research. We have presented an implementation of generalized HS-SST for AID modeling from isotropic textured surfaces that utilizes the height profile data and refractive indices. Detailed comparison of these results with actual measurements shows remarkable general agreement, while also revealing two possible limitations of scalar scattering theory, which we examined in detail. Firstly, there was a consistent decrease of wide-angle scattering in rougher textures with small lateral features, that could be explained by an effective decrease in height profile due to the onset effective medium effects. This limitation of scalar scattering theory modeling could also point out to a physical limitation of achievable high-angle scattering inside thin absorber materials using surface texturing. Secondly, there was an increased backscattering at the expense of forward scattering, especially for oblique incidence, which was experimentally linked to the presence of secondary interactions at the surface, that serve to redistribute part of the scattered power.

In a future work, we plan to investigate how the element-by-element reconstruction method that is required for generalized HS-SST can be used to calculate the so-far-neglected near-field terms of Rayleigh-Sommerfeld diffraction integral to produce AID modeling in the near field, which is an important factor to understand the origin of absorption performance inside thin-film devices. We expect this work to contribute in facilitating effective light management for photonics devices such as thin-film solar cells.

ACKNOWLEDGMENTS

We would like to thank Dr. Ibrahim Çam and METU Central Laboratories for the AFM images.

[1] J. C. Stover, *Optical Scattering: Measurement and Analysis*, 3rd ed. (SPIE Press, Bellingham, WA, 2012).
[2] L. Tsang, G. T. J. Kong, and R. Shin, *Theory of Microwave Remote Sensing* (Wiley-Interscience, New York, 1985).
[3] J. E. Harvey, K. L. Lewotsky, and A. Kotha, Effects of surface scatter on the optical performance of x-ray synchrotron beamline mirrors, Appl. Opt. **34**, 3024 (1995).
[4] J. E. Harvey, N. Choi, S. Schroeder, and A. Duparré, Total integrated scatter from surfaces with arbitrary roughness, correlation widths, and incident angles, Opt. Eng. **51**, 013402 (2012).
[5] J. E. Harvey, N. Choi, A. Krywonos, G. L. Peterson, and M. E. Bruner, Image degradation due to scattering effects in two-mirror telescopes, Opt. Eng. **49**, 063202 (2010).
[6] N. Holzschuch and R. Pacanowski, A two-scale microfacet reflectance model combining reflection and diffraction, ACM Trans. Graphics **36**, 12 (2017).
[7] R. P. Breault, *Handbook of Optics* (McGraw-Hill, New York, 1994).
[8] M. Python, E. Vallat-Sauvain, J. Bailat, D. Domine, L. Fesquet, A. Shah, and C. Ballif, Relation between substrate surface morphology and microcrystalline silicon solar cell performance, J. Non-Cryst. Solids **354**, 2258 (2008).
[9] S. O. Rice, Reflection of electromagnetic waves from slightly rough surfaces, Commun. Pure Appl. Math. **4**, 351 (1951).
[10] J. M. Elson and J. M. Bennett, Vector scattering theory, Opt. Eng. **18**, 116 (1979).
[11] E. L. Church and J. M. Zavada, Residual surface roughness of diamond-turned optics, Appl. Opt. **14**, 1788 (1975).
[12] E. L. Church, H. A. Jenkinson, and J. M. Zavada, Measurement of the finish of diamond-turned metal surfaces by differential light scattering, Opt. Eng. **16**, 360 (1977).
[13] E. L. Church, H. A. Jenkinson, and J. M. Zavada, Relationship between surface scattering and microtopographic features, Opt. Eng. **18**, 125 (1979).
[14] P. Beckmann and A. Spizzichino, *The Scattering of Electromagnetic Waves from Rough Surfaces* (Pergamon, New York, 1963).
[15] G. C. Brown, V. Celli, M. Haller, and A. Marvin, Vector theory of light scattering from a rough surface: Unitary and reciprocal expansions, Surf. Sci. **136**, 381 (1984).
[16] A. Soubret, G. Berginc, and C. Bourrely, Application of reduced Rayleigh equations to electromagnetic wave scattering by two-dimensional randomly rough surfaces, Phys. Rev. B **63**, 245411 (2001).
[17] A. R. McGurn, A. A. Maradudin, and V. Celli, Localization effects in the scattering of light from a randomly rough grating, Phys. Rev. B **31**, 4866 (1985).
[18] J. J. Greffet, Scattering of electromagnetic waves by rough dielectric surfaces, Phys. Rev. B **37**, 6436 (1988).
[19] I. Simonsen, Å. Larsen, E. Andreassen, E. Ommundsen, and K. Nord-Varhaug, Haze of surface random systems: An approximate analytic approach, Phys. Rev. A **79**, 063813 (2009).
[20] J.-P. Banon, Ø. S. Hetland, and I. Simonsen, Physics of polarized light scattering from weakly rough dielectric surfaces: Yoneda and Brewster scattering phenomena, Phys. Rev. A **99**, 023834 (2019).

[21] C. K. Carniglia, Scalar scattering theory for multilayer optical coatings, Opt. Eng. **18**, 104 (1979).
[22] H. E. Bennett and J. O. Porteus, Relation between surface roughness and specular reflectance at normal incidence, J. Opt. Soc. Am. **51**, 123 (1961).
[23] M. Zeman, R. A. C. M. M. van Swaaij, J. W. Metselaar, and R. E. I. Schropp, Optical modeling of a-Si:H solar cells with rough interfaces: Effect of back contact and interface roughness, J. Appl. Phys. **88**, 6436 (2000).
[24] J. Krč, M. Zeman, F. Smole, and M. Topič, Optical modeling of a-Si:H solar cells deposited on textured glass/SnO2 substrates, J. Appl. Phys. **92**, 749 (2002).
[25] J. Krc, F. Smole, and M. Topic, Analysis of light scattering in amorphous Si:H solar cells by a onedimensional semicoherent optical model, Prog. Photovoltaics **11**, 15 (2003).
[26] S. Schröder, A. Duparré, L. Coriand, A. Tünnermann, D. H. Penalver, and J. E. Harvey, Modeling of light scattering in different regimes of surface roughness, Opt. Express **19**, 9820 (2011).
[27] S. C. Kim, Simulation of rough surface of CIGS (CuInGaSe) solar cell by RCWA (rigorous coupled wave analysis) considering the incoherency of light, J. Opt. Soc. Korea **18**, 180 (2014).
[28] C. Rockstuhl, S. Fahr, F. Lederer, K. Bittkau, T. Beckers, and R. Carius, Local versus global absorption in thin-film solar cells with randomly textured surfaces, Appl. Phys. Lett. **93**, 061105 (2008).
[29] C. Rockstuhl, S. Fahr, K. Bittkau, T. Beckers, R. Carius, F.-J. Haug, T. Söderström, C. Ballif, and F. Lederer, Comparison and optimization of randomly textured surfaces in thin-film solar cells, Opt. Express **18**, A335 (2010).
[30] M. Sever, J. Krč, A. Čampa, and M. Topič, Rigorous modelling of light scattering in solar cells based on finite element method and Huygens' expansion, Opt. Express **23**, A1549 (2015).
[31] I. Simonsen, A. A. Maradudin, and T. A. Leskova, Scattering of electromagnetic waves from two-dimensional randomly rough perfectly conducting surfaces: The full angular intensity distribution, Phys. Rev. A **81**, 013806 (2010).
[32] T. Nordam, P. A. Letnes, and I. Simonsen, Numerical simulations of scattering of light from two-dimensional rough surfaces using the reduced Rayleigh equation, Front. Phys. **1**, 1 (2013).
[33] P. A. Letnes, A. A. Maradudin, T. Nordam, and I. Simonsen, Calculation of the Mueller matrix for scattering of light from two-dimensional rough surfaces, Phys. Rev. A **86**, 031803(R) (2012).
[34] Ø. S. Hetland, A. A. Maradudin, T. Nordam, and I. Simonsen, Numerical studies of the scattering of light from a two-dimensional randomly rough interface between two dielectric media, Phys. Rev. A **93**, 053819 (2016).
[35] Ø. S. Hetland, A. A. Maradudin, T. Nordam, P. A. Letnes, and I. Simonsen, Numerical studies of the transmission of light through a two-dimensional randomly rough interface, Phys. Rev. A **95**, 043808 (2017).
[36] J. E. Harvey, Light scattering characteristics of optical surfaces, Ph.D. dissertation, University of Arizona, 1976.
[37] J. E. Harvey, Fourier treatment of nearfield scalar diffraction theory, Am. J. Phys. **47**, 974 (1979).
[38] J. E. Harvey, C. L. Vernold, A. Krywonos, and P. L. Thompson, Diffracted radiance: a fundamental quantity in nonparaxial scalar diffraction theory, Appl. Opt. **38**, 6469 (1999).
[39] J. E. Harvey, A. Krywonos, and D. Bogunovic, Nonparaxial scalar treatment of sinusoidal phase gratings, J. Opt. Soc. Am. A **23**, 858 (2006).
[40] A. Krywonos, J. E. Harvey, and N. Choi, Linear systems formulation of scattering theory for rough surfaces with arbitrary incident and scattering angles, J. Opt. Soc. Am. A **28**, 1121 (2011).
[41] N. Sahraei, K. Forberich, S. Venkataraj, A. G. Aberle, and M. Peters, Analytical solution for haze values of aluminium-induced texture (AIT) glass superstrates for a-Si:H solar cells, Opt. Express **22**, A53 (2014).
[42] D. Dominé, F.-J. Haug, C. Battaglia, and C. Ballif, Modeling of light scattering from micro- and nanotextured surfaces, J. Appl. Phys. **107**, 044504 (2010).
[43] K. Jäger, M. Fischer, R. A. C. M. M. van Swaaij, and M. Zeman, A scattering model for nano-textured interfaces and its application in opto-electrical simulations of thin-film silicon solar cells, J. Appl. Phys. **111**, 083108 (2012).
[44] T. Lanz, B. Ruhstaller, C. Battaglia, and C. Ballif, Extended light scattering model incorporating coherence for thin-film silicon solar cells, J. Appl. Phys. **110**, 033111 (2011).
[45] T. Lanz, K. Lapagna, S. Altazin, M. Boccard, F.-J. Haug, C. Ballif, and B. Ruhstaller, Light trapping in solar cells: numerical modeling with measured surface textures, Opt. Express **23**, A539 (2015).
[46] D. Dominé, The role of front electrodes and intermediate reflectors in the optoelectronic properties of high-efficiency micromorph solar cells, Ph.D. dissertation, Université de Neuchâtel, 2009.
[47] F.-J. Haug, M. Bräuninger, and C. Ballif, Fourier light scattering model for treating textures deeper than the wavelength, Opt. Express **25**, A14 (2017).
[48] D. Nečas and P. Klapetek, Gwyddion: an open-source software for SPM data analysis, Cent. Eur. J. Phys. **10**, 181 (2012).
[49] H. Cui, P. J. Gress, P. R. Campbell, and M. Green, Developments in the aluminium induced texturing (AIT) glass process, Glass Technol.: Eur. J. Glass Sci. Technol., Part A **53**, 158 (2012).
[50] M. Ünal, H. Nasser, M. Günöven, I. Sökmen, A. Tankut, and R. Turan, Effect of aluminum thickness and etching time of aluminum induced texturing process on soda lime glass substrates for thin solar cell applications, Phys. Status Solidi C **12**, 1201 (2015).
[51] M. Ünal, A. Tankut, S. Canlı, and R. Turan, Near-unity haze by aluminum induced glass texturing: structural evolution of Al/glass interface and its impact on texturing, Opt. Mater. Express **7**, 3051 (2017).
[52] H. Nasser, E. Özkol, A. Bek, and R. Turan, High haze nature of textured Al:ZnO with Ag nanoparticles for light management in thin film solar cells, Opt. Mater. Express **5**, 932 (2015).
[53] J. W. Goodman, *Introduction to Fourier Optics*, 3rd ed. (Roberts & Company Publishers, Englewood, CO, 2004).